Entropy **2013**, *15*, 5012-5021; doi:10.3390/e15115012

OPEN ACCESS

entropy

ISSN 1099-4300

www.mdpi.com/journal/entropy

Article

Microstructures and Mechanical Properties of $TiCrZrNbN_x$ Alloy Nitride Thin Films

Chun-Huei Tsau * and Yu-Hsin Chang

Institute of Nanomaterials, Chinese Culture University, Taipei 111, Taiwan;
E-Mail: mibeking@gmail.com

* Author to whom correspondence should be addressed; E-Mail: chtsau@staff.pccu.edu.tw;
Tel.: +886-2-28610511 (ext. 33605).

Received: 20 September 2013; in revised form: 10 November 2013 / Accepted: 13 November 2013 / Published: 18 November 2013

Abstract: The pure elements Ti, Zr, Cr, Nb were selected to produce an TiCrZrNb alloy target and deposited thin films thereof by a reactive high vacuum DC sputtering process. Nitrogen was used as the reactive gas to deposit the nitride thin films. The effect of nitriding on the properties of the $TiCrZrNbN_x$ film was tested by changing the nitrogen ratio of the atmosphere. All of the as-deposited $TiCrZrNbN_x$ nitride films exhibited an amorphous structure. The film thickness decreases by increasing the N_2 flow rate, because the Ar flow rate decreased and the target was poisoned by nitrogen. The hardness and Young's modulus were also measured by a nano-indenter. The hardness and Young's modulus of the $TiCrZrNbN_x$ nitride films were all lower than those of a TiCrZrNb metallic film.

Keywords: $TiCrZrNbN_x$; nitride film; microstructure; deposition rate; hardness; Young's modulus

1. Introduction

The concept of high-entropy alloys was introduced by Yeh [1–2], using multi-principal element alloys to replace only one principal element in traditional alloys, such as steel, bronze and aluminum alloys. In this way the properties of the high-entropy alloys would not be dominated by any one element. Yeh also explicitly explained the four core effects of the high-entropy alloys: high entropy, sluggish diffusion, severe lattice distortion, and cocktail. This would lead the alloy design concept to a new field,

and also extend the applications. As a result, more and more researchers agreed with this high-entropy alloy concept, and started to investigate high-entropy alloys [3–6].

Titanium nitride has been used for surface coating because of its good mechanical properties and corrosion resistance [7,8]. Adding chromium to form a TiCrN ternary system could also further enhance corrosion resistance [9]. The zirconium nitride thin film also could improve the corrosion resistance of 316 L stainless steel [10]. The niobium nitride thin film was deposited on the surface of SKD11 tool steel [11], and its hardness could be increased by controlling the deposition parameters, such as temperature and bias. High-entropy alloy nitride thin films were also studied in recent years [12,13]. The present study selected titanium, chromium, zirconium and niobium to prepare the target, and then deposited the alloy nitride thin films to investigate their properties.

2. Experimental Procedures

The equiatomic TiCrZrNb target was prepared by arc melting; the purity of all the elements used was not less than 99.9%, and the nominal weight percents of Ti, Cr, Zr and Nb were 16.9%, 18.3%, 32.1% and 32.7%, respectively. A DC reactive sputtering without bias operated at 100 W was used to deposit $TiCrZrNbN_x$ films, and the flow rate of Ar + N_2 was fixed at 30 sccm. The distance from the target to substrate holder is about 12 cm. Films were deposited on Si (100) wafer and SiO_2/Si substrates which were cleaned sequentially in DI water, acetone and DI water before coating in the sputtering system. A shutter placed between the magnetron and the substrate holder allowed the substrates and target to be pre-sputtered before the film deposition. The pre-sputtering time was fixed at 10 min. The base and deposition pressure were 5×10^{-5} and 2×10^{-3} torr, respectively. No temperature control system was used during deposition. The deposition times depended on the deposition rate. All the tests were done on the 1 micrometer thickness thin films.

The phases of the TiCrZrNb target were identified with a Bruker AXS X-ray diffraction (XRD) diffractometer (Bruker, Billerica, MA, USA); and the $TiCrZrNbN_x$ thin films were identified by a MAC Science MXP18 X-ray diffractometer (MAC Science, Yolohama, Japan) with a glancing angle of 2 degree. The microstructural evolution for the $TiCrZrNbN_x$ films was followed by scanning electron microscopy (SEM) and transmission electron microscopy (TEM). SEM observation was performed with a JEOL JSM-6335 field emission scanning electron microscope (JEOL, Tokyo, Japan) operated at 15 kV. TEM observation was performed with a JEOL JEM-2010 transmission electron microscope operated at 200 kV. The compositions of the thin films were measured by a JEOL JXA-8800 electron probe microanalysis (EPMA) operated at 15 kV. The hardness and Young's modulus of the thin films with 1 micrometer thickness was measured by a NanoTest 600 nanoindenter (Micro Materials Limited, Wrecsam, UK) with a load of 3 mN, and each specimen was tested more than five times.

3. Results and Discussion

The as-cast TiCrZrNb alloy (the target) had a dendritic microstructure, as shown in Figure 1. The dendrite shows only a single phase, and the interdendritic region shows an eutectic structure. Figure 2 is the XRD diffraction pattern of this as-cast TiCrZrNb alloy, and it indicates that there are two phases existing in this alloy. By comparing the intensities of the XRD peaks and the SEM micrographs, the dendrite was a HCP phase with lattice constants of a = 0.297 nm and c = 0.479 nm.

The matrix of the interdendritic region was a BCC phase with a lattice constant of 0.298 nm. The lattice constants of the HCP phase were calculated from the peaks of (100) and (002); and the lattice constant of the BCC phase was calculated from the (110) peak. The structure of the particles embedded in the matrix of interdendritic region was HCP phase and had a similar dendritic structure.

Figure 1. SEM micrograph of as-cast TiCrZrNb alloy.

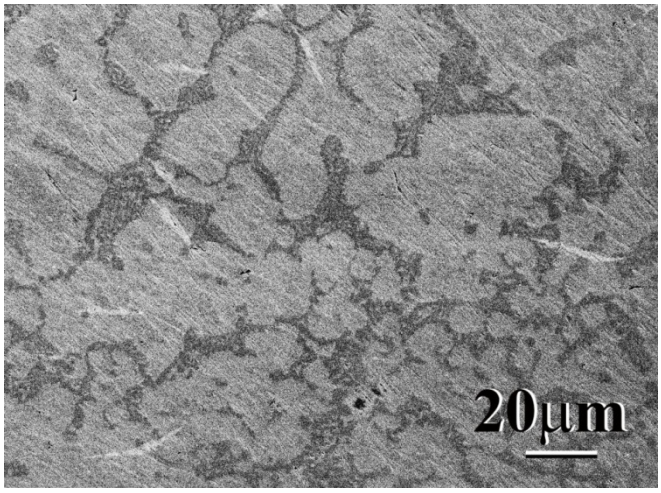

Figure 2. XRD diffraction pattern of as-cast TiCrZrNb alloy.

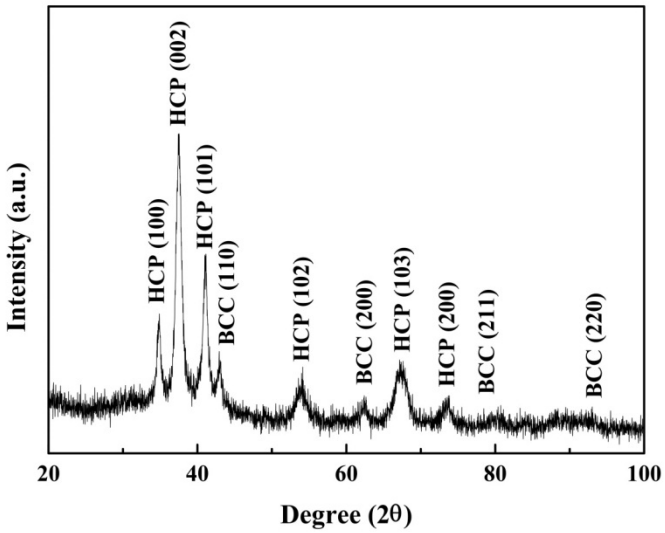

This study produced alloy nitride thin films of this TiCrZrNb alloy target with a mixing gas of Ar and N_2. The total amount of Ar and N_2 were fixed at 30 sccm, and flow rate of N_2 was varied from 2 to 10 sccm. Figure 3 indicates some top view and corresponding cross-section SEM micrographs of the as-deposited TiCrZrNb metallic thin films and $TiCrZrNbN_x$ nitride thin films. The deposition time of these thin films shown in Figure 3 was 1 h. The metallic thin film was deposited while the atmosphere was Ar, that is, the flow rate of N_2 was zero. All of the top view micrographs of $TiCrZrNbN_x$ thin films show a particle-like structure. Although these micrographs looked like granular structures, they actually had an amorphous structure. The deposition rate against the N_2 flow rate is shown in Figure 4. The deposition rate decreased sharply result upon increasing the N_2 flow rate. The decreasing

deposition rate was contributed by two factors. One was caused by the decreasing Ar flow rate. Reducing the flow rate of Ar also diminished the sputtering yield, and consequently the deposition rate decayed. The other factor was a so-called poisoning phenomenon, because some insulator was forming on the surface of the target [14,15].

Figure 3. SEM micrographs of as-deposited $TiCrZrNbN_x$ thin films (deposition time was 1 h): (**a**) top view, N_2 flow rate: 0 sccm; (**b**) cross-section, N_2 flow rate: 0 sccm; (**c**) top view, N_2 flow rate: 2 sccm; (**d**) cross-section, N_2 flow rate: 2 sccm; (**e**) top view, N_2 flow rate: 6 sccm; (**f**) cross-section, N_2 flow rate: 6 sccm; (**g**) top view, N_2 flow rate: 8 sccm; (**h**) cross-section, N_2 flow rate: 8 sccm. The cracks are marked by arrows.

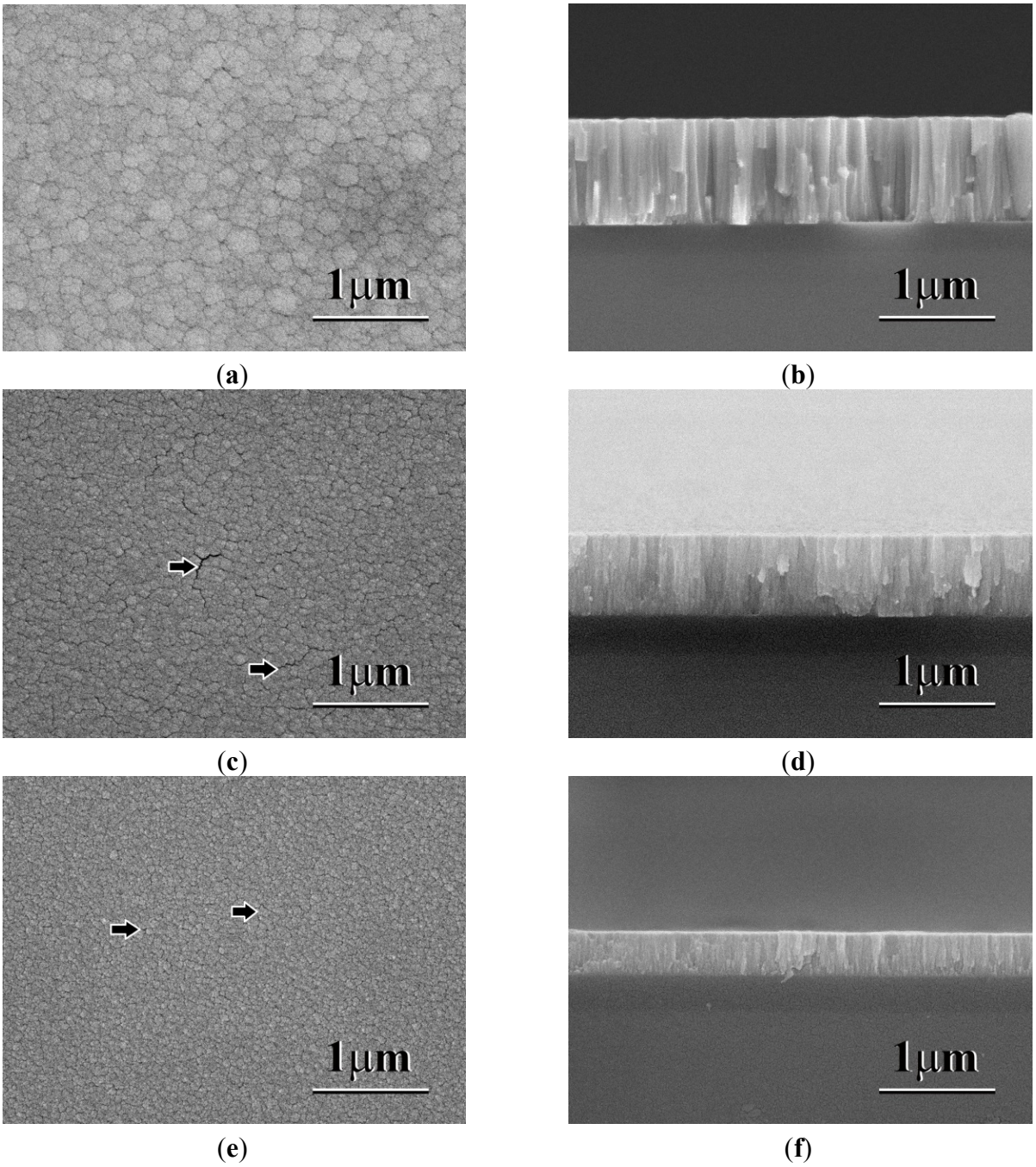

(**a**) (**b**) (**c**) (**d**) (**e**) (**f**)

Figure 3. *Cont.*

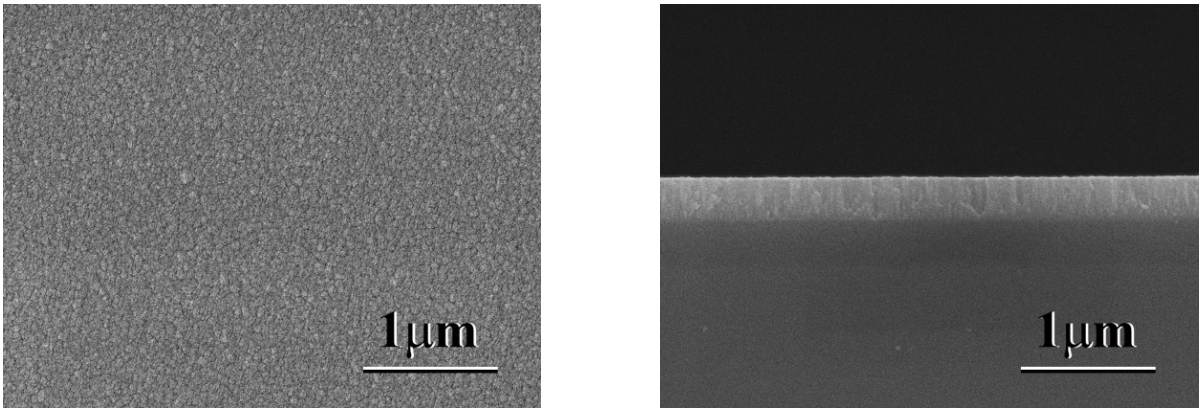

(**g**) (**h**)

Figure 4. Plot of the deposition rate of as-deposited $TiCrZrNbN_x$ thin films *vs.* N_2 flow rate. Total gas (Ar and N_2) flow rate was fixed at 30 sccm.

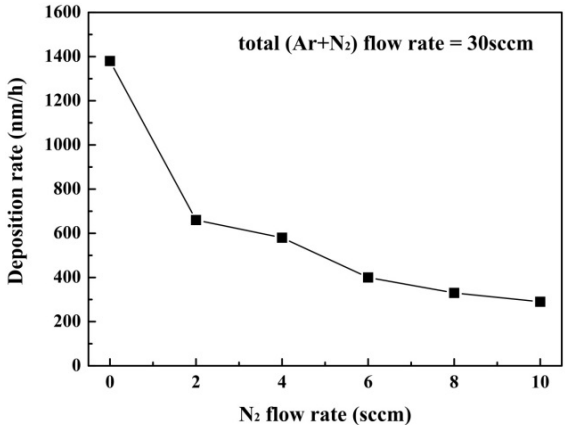

The structures of the $TiCrZrNbN_x$ thin films were identified by XRD, as shown in Figure 5. No evident peak is observed from the XRD patterns. Therefore, it indicated that all of the as-deposited TiCrZrNb alloy film and $TiCrZrNbN_x$ nitride films were amorphous. The central line of the broad peak shifts gradually to a smaller angle side revealing that the average interatomic spacing becomes larger with more nitrogen doping. Moreover, the XRD patterns of the $TiCrZrNbN_x$ films with N_2 flow rate of 8 and 10 sccm were very similar; this indicated that the solid solubility of nitrogen was saturated when the N_2 flow rate reached 8 sccm. The amorphous structure was also confirmed by TEM observation. Figure 6 shows the TEM bright field (BF) images and the corresponding selection area diffraction patterns (SAD) of the as-deposited thin films. Figure 6a shows the TEM image of the as-deposited TiCrZrNb metallic thin film; and the TEM images of as-deposited $TiCrZrNbN_x$ nitride thin films under N_2 flow rate of 2, 4 and 10 sccm are shown in Figure 6b–d, respectively. All of the TEM images show the columnar structures but differ in sizes. All of the corresponding SADs indicate that their structures are amorphous. The columnar amorphous boundaries were the results of a void network [16,17]. Donovan and Heineman first observed these boundaries in an evaporated amorphous Ge thin film [16], and they suggested that the formation of a void network resulted in density-deficient boundaries that are intrinsic to amorphous films. Tsukimoto *et al.* [17] further described the mechanism of formation of amorphous grain boundaries in TaN thin films, following a detailed analysis.

Figure 5. XRD patterns of of as-deposited $TiCrZrNbN_x$ thin films under different N_2 flow rates.

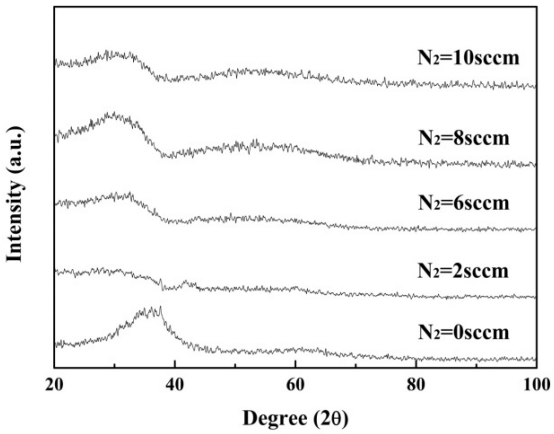

Figure 6. TEM micrographs and their corresponding diffraction patterns of as-deposited $TiCrZrNbN_x$ thin films under N_2 flow rates of: (**a**) 0 sccm; (**b**) 2 sccm; (**c**) 4 sccm; and (**d**) 10 sccm.

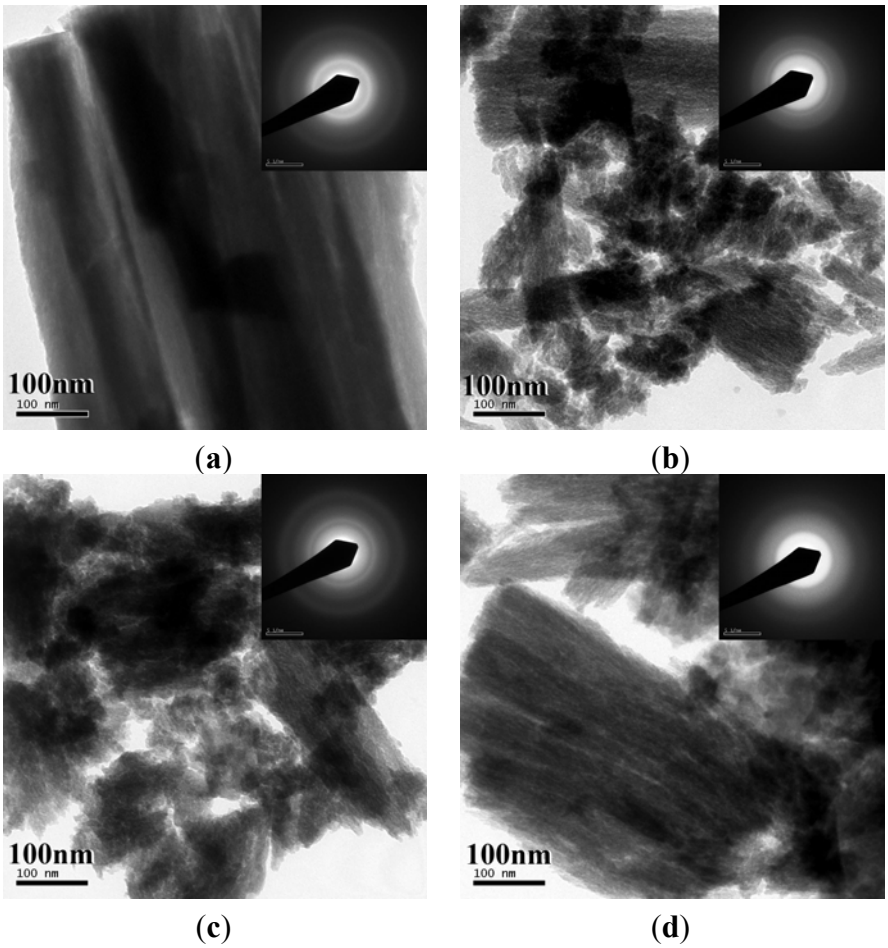

The diameters of Ti, Cr, Zr and Nb atoms are 0.294 nm, 0.256 nm, 0.320 nm and 0.294 nm, respectively [18]. The Zr atom is 8.8% larger than the Ti and Nb atoms; and it is 25% larger than the Cr atom. The composition of the alloy film was uniform because not only the deposition was an atom-by-atom process but also the confusion principle dictated that four elements with different crystalline structures could not form a vital crystal structure without sufficient time and energy for

diffusion. The amorphization could be explained by the variation among the atomic sizes of these four elements, and the defects, and the effect of the confusion principle, as stated above. The broad peak broadened after increasing of nitrogen; this indicated that the amorphous structure became more disordered with more nitrogen doping. These phenomena could be explained based on the occupation of small nitrogen atoms in the interstitial sites. The nitrogen atoms were always larger than the interstitial sites, the interatomic spacing would be thus enlarged, and atomic configuration structure would be more distorted.

The compositions of the as-deposited $TiCrZrNbN_x$ thin films are shown in Figure 7. The contents of the Ti, Cr, Zr and Nb in the as-deposited TiCrZrNb thin films were around 25 atom percent. This also proved the compositions of the TiCrZrNb target. The nitrogen contents in the $TiCrZrNbN_x$ thin films were very small under the low N_2 flow rate regime. The nitrogen contents in the $TiCrZrNbN_x$ thin films increased significantly when the N_2 flow rate was greater than 4 sccm. The nitrogen contents in the $TiCrZrNbN_x$ thin film saturated at about 47 atomic percent when the N_2 flow rate reached 8 sccm. This also proves the results of XRD patterns described above.

Figure 7. Plot of the compositions of the $TiCrZrNbN_x$ thin films *vs.* N_2 flow rate.

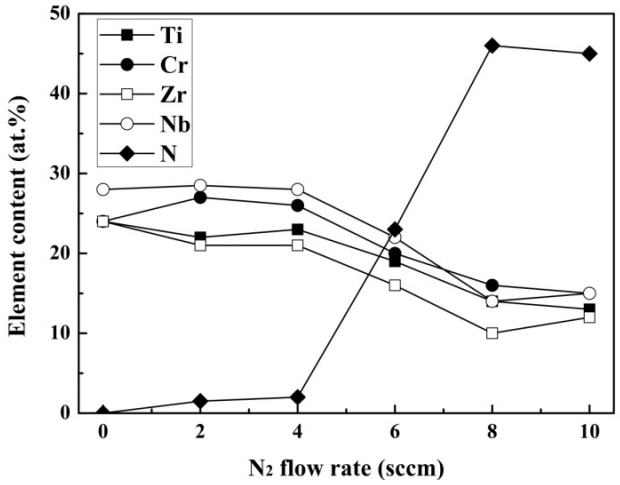

Hardness and Young's modulus of the as-deposited $TiCrZrNbN_x$ thin films with 1 micrometer thickness were tested by a nanoindenter, and the typical nanoindentation load-displacement loading curves are shown in Figure 8. The left curve in Figure 8 is the loading curve; and the right curve is the unloading curve. The maximum load shows 3 mN. The stiffness of a material can be obtained from the initial unloading slope by evaluating the maximum load and maximum depth. The details of testing and calculating Young's modulus and hardness can be found in Fang and Chang's work [19].

The hardness and Young's modulus of the as-deposited $TiCrZrNbN_x$ thin films were shown in Figures 9a,b respectively. Hardness of the TiCrZrNb metallic thin film was 4.4 GPa. This value was very close to the hardness of TiCrZrNb bulk, 4.7 GPa. The difference of hardness between the bulk and thin film was because of their different structures. The TiCrZrNb bulk had a dense crystalline structure; the TiCrZrNb thin film had an amorphous structure, and this structure was not as dense as that of the bulk, as described above. Additionally, some cracks were observed along the particle boundaries after increasing the N_2 flow rate; these were caused by the thermal stress or internal stress during the deposition, because the substrate was cool during deposition. Therefore, hardness of the $TiCrZrNbN_x$ thin films decreased due to the cracks. However, more study on the relationship between the cracks and nitrogen flow rate is

needed. The cracks almost vanished when the N_2 flow rate reached 8 sccm, and the hardness of the $TiCrZrNbN_x$ thin films thereby increased again. The Young's modulus of the as-deposited TiCrZrNb thin film was 122 GPa. This value indicated that this thin film is a soft material, and this value was only slightly higher than the Young's modulus of phosphor bronze, 110 GPa [20].

Figure 8. Typical nanoindentation load-displacement loading curves on the $TiCrZrNbN_x$ thin films under a N_2 flow rate of 4 sccm.

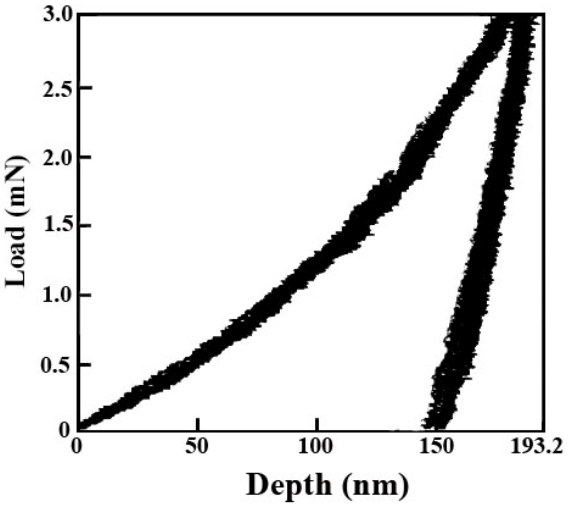

Figure 9. Plots of (**a**) hardness, and (**b**) Young's modulus of the $TiCrZrNbN_x$ thin films *vs.* N_2 flow rate.

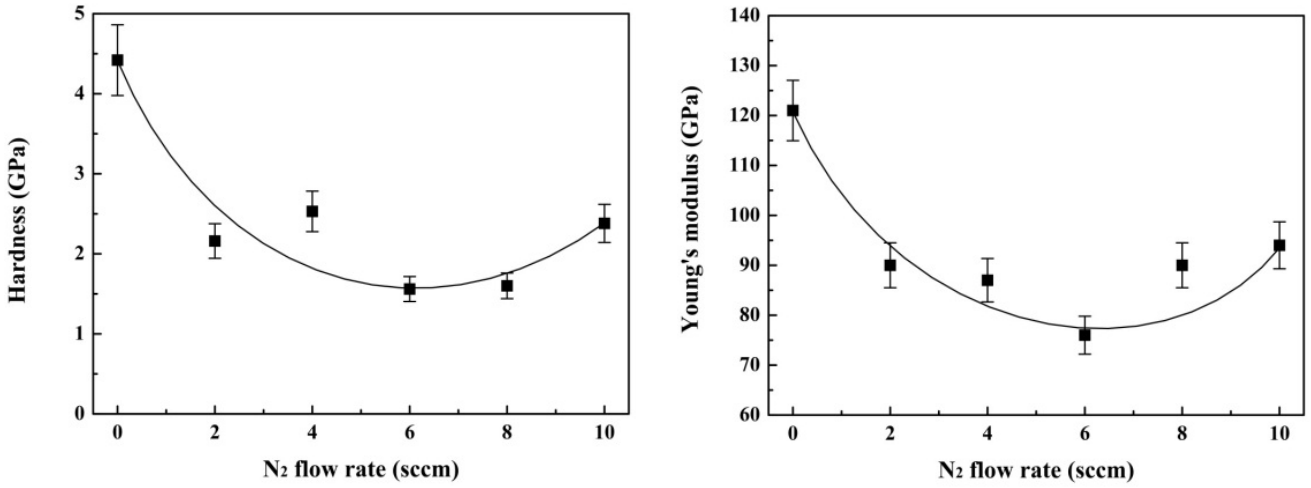

(**a**) (**b**)

Moreover, the Young's modulus of the $TiCrZrNbN_x$ thin films decreased with increasing the N_2 flow rate, just like the hardness tendency. The Young's modulus of the $TiCrZrNbN_x$ thin films increased again after the N_2 flow rate increased to 8 sccm. The Young's modulus (E) and hardness (H) of the $TiCrZrNbN_x$ thin films have almost the same tendency, and H/E is about 0.06 as shown in Figure 10. Jiang *et al.* investigated hardness and Young's modulus of amorphous hydrogenated carbon and silicon films, and pointed out that the hardness of amorphous hydrogenated carbon and silicon films are proportional to Young's modulus, that is $(H/E)_C = 0.115$ and $(H/E)_{Si} = 0.093$ [21]. This work also exhibited a similar result, but the H/E value was lower.

Figure 10. Plot of correlation between hardness and Young's modulus of the $TiCrZrNbN_x$ thin films.

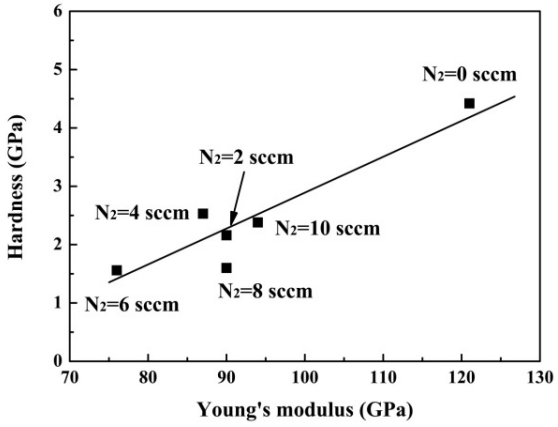

4. Conclusions

The equiatomic TiCrZrNb alloy target was made by arc-melting, and the TiCrZrNb metallic film and $TiCrZrNbN_x$ nitride films were successfully produced by reactive DC sputtering. The XRD and TEM analysis results indicated that all of the as-deposited thin films had a columnar amorphous structure. The deposition rate of the $TiCrZrNbN_x$ thin films would decrease when the N_2 flow rate increased, because the Ar flow rate decreased and the target was poisoned by nitrogen. The nitrogen-content in the $TiCrZrNbN_x$ thin films increased sharply after the N_2 flow rate was more than 4 sccm; and nitrogen-content in the $TiCrZrNbN_x$ thin films was saturated at about 47 atomic percent when the N_2 flow rate reached 8 sccm. The results of hardness and Young's modulus test indicated that the $TiCrZrNbN_x$ thin films were softer than TiCrZrNb metallic film.

Conflicts of Interest

The authors declare no conflict of interest.

References

1. Yeh, J.W.; Chen, S.K.; Gan, J.Y.; Chin, T.S.; Shun, T.T.; Tsau, C.H.; Chang, S.Y. High-entropy alloys with multi-principal elements: Novel alloy design concepts and outcomes. *Adv. Eng. Mater.* **2004**, *6*, 299–303.
2. Yeh, J.W. Recent progess in high-entropy alloys. *Ann. Chim.—Sci. Mater.* **2006**, *31*, 633–648.
3. Braic, V.; Vladescu, A.; Balaceanu, M.; Luculescu, C.R.; Braic, M. Nanostructured multi-element (TiZrNbHfTa)N and (TiZrNbHfTa)C hard coatings. *Surf. Coat. Tech.* **2012**, *211*, 117–121.
4. Wang, F.J.; Zhang, Y. Effect of Co addition on crystal structure and mechanical properties of $Ti_{0.5}$CrFeNiAlCo high entropy alloy. *Mater. Sci. Eng. A* **2008**, *496*, 214–216.
5. Praveen, S.; Murty, B.S.; Kottada, R.S. Alloying behavior in multi-component AlCoCrCuFe and NiCoCrCuFe high entropy alloys. *Mater. Sci. Eng. A* **2012**, *534*, 83–89.
6. Wang, Y.P.; Li, B.S.; Ren, M.X.; Yang, C.; Fu, H.Z. Microstructure and compressive properties of AlCrFeCoNi high entropy alloy. *Mater. Sci. Eng. A* **2008**, *491*, 154–158.

7. Chou, W.J.; Yu, G.P.; Huang, J.H. Mechanical properties of TiN thin film coatings on 304 stainless steel substrates. *Surf. Coat. Tech.* **2002**, *149*, 7–13.
8. Ren, C.S.; Mu, Z.X.; Wang, Y.N.; Yu, H. Corrosion behavior of TiN films prepared by vacuum arc deposition and nitrogen ion beam dynamic mixing implantation. *Surf. Coat. Tech.* **2004**, *185*, 210–214.
9. Nam, N.D.; Jo, D.S.; Kim, J.G.; Yoon, D.H.O. Corrosion protection of CrN/TiN multi-coating for bipolar plate of polymer electrolyte membrane fuel cell. *Thin Solid Films* **2011**, *20*, 6787–6791.
10. Hubler, R.; Cozza, A.; Marcondes, T.L.; Souza, R.B.; Fiori, F.F. Wear and corrosion protection of 316-L femoral implants by deposition of thin films. *Surf. Coat. Tech.* **2001**, *142–144*, 1078–1083.
11. Kim, S.K.; Cha, B.C.; Yoo, J.S. Deposition of NbN thin films by DC magnetron sputtering process. *Surf. Coat. Tech.* **2004**, *177–178*, 434–440.
12. Cheng, K.H.; Lai, C.H.; Lin, S.J.; Yeh, J.W. Structural and mechanical properties of multi-element $(AlCrMoTaTiZr)N_x$ coatings by reactive magnetron sputtering. *Thin Solid Films* **2011**, *519*, 3185–3190.
13. Hsueh, H.T.; Shen, W.J.; Tsai, M.H.; Yeh, J.W. Effect of nitrogen content and substrate bias on mechanical and corrosion properties of high-entropy films $(AlCrSiTiZr)_{100-x}N_x$. *Surf. Coat. Tech.* **2012**, *206*, 4106–4112.
14. Machet, J.; Combadiere, L. Study and control of both target-poisoning mechanisms and reactive phenomenon in reactive planar magnetron cathodic sputtering of TiN. *Surf. Coat. Tech.* **1996**, *82*, 145–157.
15. Waite, M.M.; Shah, S.I. Target poisoning during reactive sputtering of silicon with oxygen and nitrogen. *Mater. Sci. Eng. B* **2007**, *140*, 64–68.
16. Donovan, T.S.; Heinemann, K. High-resolution electron microcope observation of voids in amorphous Ge. *Phys. Rev. Lett.* **1971**, *27*, 1794–1796.
17. Tsukimoto, S.; Moriyama, M.; Murakami, M. Microstructure of amorphous tantalum nitride thin films. *Thin Solid Films* **2004**, *460*, 222–226.
18. Smith, W.F. *Foundations of Materials Science and Engineering*, 3rd ed.; MaGraw-Hill, Inc.: New York, NY, USA, 2004; p.877.
19. Fang, T.H.; Chang, W.J. Nanomechanical properties of copper thin films on different substrates using the nanoindentation technique. *Microelectron. Eng.* **2003**, *65*, 231–238.
20. Beer, F.P.; Johnston, E.R., Jr. *Mechanics of Materials*; McGraw-Hill, Inc.: New York, NY, USA, 1987; p.585.
21. Jiang, X.; Reichelt, K.; Stritzker, B. The hardness and Young's modulus of amorphous hydrogenated carbon and silicon films measured with an ultralow load indenter. *J. Appl. Phys.* **1989**, *66*, 5805–5808.